

Evidence of Nanocrystalline Semiconducting Graphene Monoxide during Thermal Reduction of Graphene Oxide in Vacuum

Eric C. Mattson,[†] Haihui Pu,[‡] Shumao Cui,[‡] Marvin A. Schofield,[†] Sonny Rhim,[†] Ganhua Lu,[‡] Michael J. Nasse,^{†,§} Rodney S. Ruoff,^{||} Michael Weinert,[†] Marija Gajdardziska-Josifovska,[†] Junhong Chen,^{*,‡} and Carol J. Hirschmugl^{*,†}

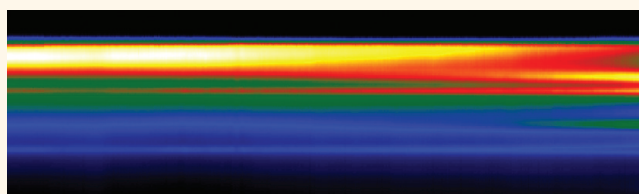
[†]Department of Physics and Laboratory for Surface Studies, University of Wisconsin—Milwaukee, Milwaukee, Wisconsin 53211, United States,

[‡]Department of Mechanical Engineering and Laboratory for Surface Studies, University of Wisconsin—Milwaukee, Milwaukee, Wisconsin 53211, United States,

[§]Synchrotron Radiation Center, Stoughton, Wisconsin 53589, United States, and ^{||}Department of Mechanical Engineering and the Texas Materials Institute, University of Texas at Austin, Austin, Texas 78712, United States

Graphene has demonstrated great potential for novel electronic technologies;^{1–3} however, many emerging applications require atomically thin films with a substantial band gap. One route toward the manipulation of the electronic properties of graphene-based materials is through chemical modification. Chemically modified graphene or graphene oxide (G-O)^{4–8} has already found various applications such as supercapacitors,⁹ sensors,^{10,11} and flexible transparent conductive electrodes.¹² However, G-O is a nonstoichiometric, partially disordered material^{13,14} with poor electronic properties. While studies have indicated that on average the hexagonal lattice constant of graphene is preserved in G-O,^{13–15} amorphous regions coexist with the crystalline carbon lattice, with a number of oxygen functional groups, such as hydroxyl, carboxyl, carbonyl, epoxide, and intercalated water,^{15–17} bonded with no long-range order.¹³ These disordered qualities of G-O make it an unappealing candidate for application in modern electronics. Thus, G-O is most commonly modified by various chemical⁶ and thermal reduction treatments^{15–17} with the goal of removing oxygen functional groups from G-O and producing graphene. While the quality of the resulting materials can in general be improved via chemical vapor deposition (CVD),¹⁸ these treatments generally fail to form graphene and produce yet another nonstoichiometric partially reduced GO where oxygen remains disordered.

ABSTRACT



As silicon-based electronics are reaching the nanosize limits of the semiconductor roadmap, carbon-based nanoelectronics has become a rapidly growing field, with great interest in tuning the properties of carbon-based materials. Chemical functionalization is a proposed route, but syntheses of graphene oxide (G-O) produce disordered, nonstoichiometric materials with poor electronic properties. We report synthesis of an ordered, stoichiometric, solid-state carbon oxide that has never been observed in nature and coexists with graphene. Formation of this material, graphene monoxide (GMO), is achieved by annealing multilayered G-O. Our results indicate that the resulting thermally reduced G-O (TRG-O) consists of a two-dimensional nanocrystalline phase segregation: unoxidized graphitic regions are separated from highly oxidized regions of GMO. GMO has a quasi-hexagonal unit cell, an unusually high 1:1 O:C ratio, and a calculated direct band gap of ~ 0.9 eV.

KEYWORDS: graphene oxide · thermal reduction · *in situ* electron diffraction · infrared spectroscopy · density functional theory · nanocrystals · semiconductors

We demonstrate the formation of a stoichiometric carbon oxide by vacuum annealing of multilayered G-O, a method commonly used to make thermally reduced graphene oxide (TRG-O). Studies of TRG-O, however, have primarily focused on reduction of monolayer or few layer systems,^{15–17} with little attention paid to thermal reduction of systems with a large number of layers. While previous reports¹⁷ have shown

* Address correspondence to
cjhirsch@uwm.edu,
jhchen@uwm.edu.

Received for review August 21, 2011
and accepted November 20, 2011.

Published online November 21, 2011
10.1021/nn203160n

© 2011 American Chemical Society

that the chemistry of intercalated water in multilayer G-O is significant, no investigations have reported the effect of vacuum annealing a large number of G-O layers to high temperature. We have found that the multilayer structure of G-O thin films with intercalated water results in a previously unobserved atomic structure and morphology when annealed in vacuum: a two-dimensional phase segregation produces graphitic regions with little or no oxidation that coexist with oxidized regions with an unusually high oxygen content. Our work, combining *in situ* selected area electron diffraction (SAED) studies with synchrotron-based infrared microspectroscopy (IRMS) and density functional theory (DFT) calculations, reveals the atomic structure of the ordered oxidized regions coexisting with unoxidized graphene-like regions. From DFT modeling guided by experimentally derived structural data, we determined that the resulting oxidized structure, Graphene Monoxide (GMO), consists of a quasi-hexagonal unit cell with two carbon atoms bridged by a double-epoxide pair. GMO formation occurs because the large number of layers effectively limits the reduction process, and conversion of the remaining oxygen functional groups to a double-epoxide-type configuration is energetically favorable. Furthermore, the resulting material demonstrates appealing transport properties, which could potentially be tuned owing to GMO's direct gap of 0.9 eV.

RESULTS AND DISCUSSION

Figure 1a compares SAED patterns of a multilayer G-O film before (left) and during (right) *in situ* vacuum annealing, at 750 °C. Before annealing, the primary features evident in Figure 1a are the diffraction rings (labeled as I and II) from spacings of 0.213 and 0.123 nm, respectively, corresponding to the {100}- and {110}-type reflections of graphene. A ring pattern is observed rather than a spot pattern due to the fact that the sample consists of a large number of randomly oriented layers (see Methods and Figure S1). Analysis of the relative intensities shows that the {100}-type reflections produce a greater diffracted intensity than the {110} reflections, indicating that the layers are monolayers with disordered stacking, as opposed to the few-layer Bernal-stacked graphite oxide.¹⁴ Moreover, SAED patterns (Figure S2, Table S1) recorded at higher scattering angles (i.e., smaller lattice spacing) clearly indicate weaker higher order rings also consistent with crystalline graphene. In addition, SAED patterns recorded before annealing (Figure 1a, left) show two broad amorphous rings centered at about 0.27 and 0.52 Å⁻¹ (0.370 and 0.185 nm in real space). The amorphous rings are attributable to the first- and second-order reflections from nearest-neighbor disordered species.

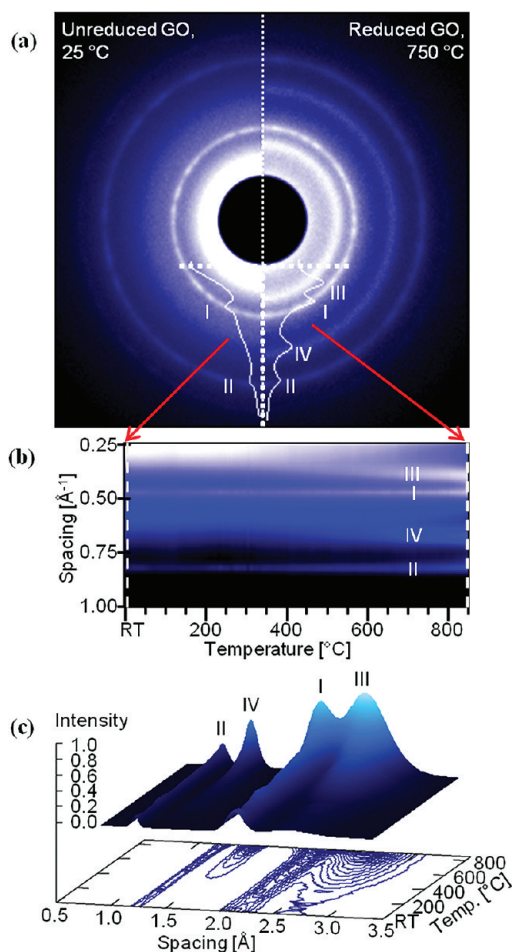


Figure 1. Evolution of Electron Diffraction patterns with temperature. (a) SAED patterns of G-O sample before (left) and after (right) vacuum reduction annealing. Overlay is the radial average of intensity showing peaks at ring positions I and II before annealing, and the addition of peaks III and IV after annealing. (b) Radially averaged profiles from SAED patterns as a function of temperature. Profiles displayed as overlay in top panel are equivalent to profiles along the corresponding dashed lines (arrowed) in middle panel of figure. Peaks III and IV evolve continuously from the broad background, most notably in the temperature range from 500 to 700 °C. (c) Temperature-dependent evolution of unwrapped SAED patterns. As temperature is increased, new peaks appear with indicated spacings and grow in intensity. Peaks I and II are attributed to graphene regions of the sample, while peaks III and IV are attributed to regions of nanocrystalline graphene monoxide.

While annealing the multilayer G-O film, two prominent rings (labeled as III and IV) develop corresponding to spacings of about 0.260 and 0.152 nm, respectively, while the graphene rings (I and II) remain largely unchanged (Figure 1a). Thus the SAED data demonstrate that a new crystalline phase develops upon annealing. A visualization of the complete temperature-dependent evolution of SAED patterns from the G-O film annealing (extracted from a real time movie; see Supplementary movie) is shown in Figure 1b. Diffraction rings in a conventional SAED pattern (Figure 1a) appear as horizontal lines in the representation of Figure 1b.

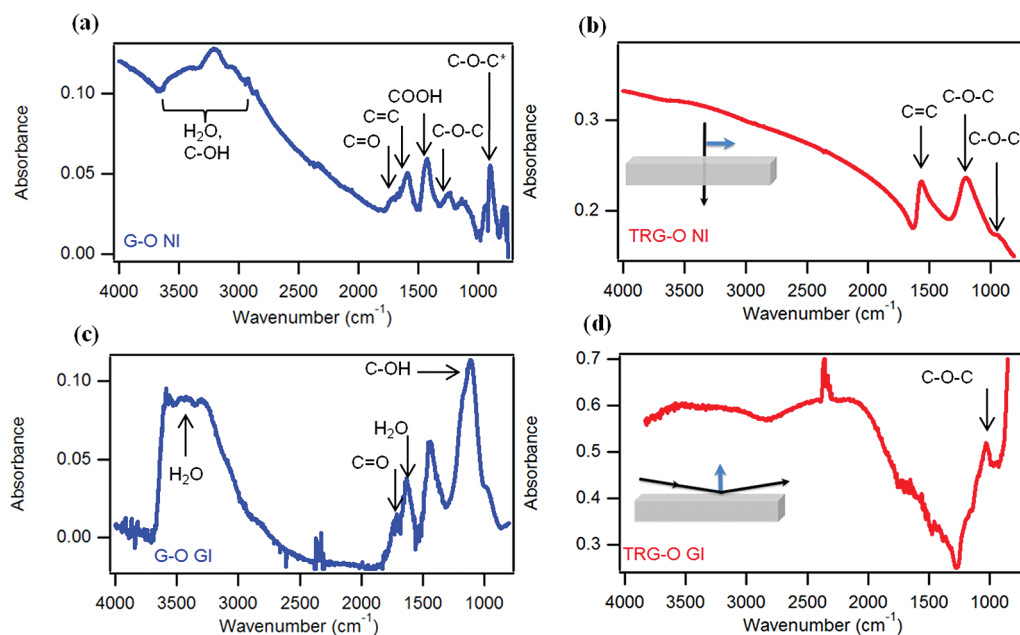


Figure 2. IRMS of G-O and TRG-O. Normal Incidence (NI) transmission probes vibrations with a dipole moment parallel to the film's basal plane as the E-field vector (blue arrow) is within this plane, while GI probes those with a dipole moment perpendicular to the basal plane. (a) NI IR absorbance of unreduced G-O with contributing functional groups assigned to spectral regions. (b) NI IR absorbance spectrum of TRG-O samples with functional groups assigned. (c) GI IR absorbance spectrum of G-O. (d) GI IR absorbance spectrum of TRG-O. In all spectra, bending/deformation modes are indicated by *.

From Figure 1b, it is evident that the graphene rings, I and II, grow in intensity as the sample is annealed but that they remain essentially fixed in reciprocal space position. The new crystalline GMO phase characterized by peaks III and IV, however, shows a qualitatively different behavior with temperature. The broad amorphous peak (associated with the disordered functional groups) initially centered at about 0.27 \AA^{-1} appears to split into two bands, one of which evolves in position and intensity into the crystalline reflection of the GMO phase labeled as III. The remaining amorphous contributions shift closer to the reciprocal space origin and suffer a dramatic reduction in intensity, most evident in the 300–500 °C temperature range, with similar behavior observed in band IV. This structural ordering does not produce visible features in bright field TEM images, indicating that the multilayer morphology is preserved and that the new phase has a 2D structure. The evolution of the SAED patterns was observed across the entire sample and was constant upon cooling the sample, thus ruling out effects related to sample drift. These observations were reproducible in numerous experiments.

To quantify the temperature evolution of the diffraction data, individual profiles of Figure 1b over the complete temperature range were fit with a set of Gaussians (see Methods and Figure S3). Figure 1c shows the fitting results for the crystalline diffraction bands I–IV without the background and amorphous contribution where several key features of the structural evolution of the G-O film are observed. First, the integrated

intensity of the graphene peaks I and II, related to the volume fraction of scattering material, more than doubles. Similarly, the integrated intensity of peaks III and IV (GMO phase) grows rapidly from zero in the starting material to more than 1.5 times that of the graphene phase at the end of the annealing. These integrated intensities may be considered in terms of qualitative increases and decreases in quantity of material, as an absolute determination of the volume fraction would require knowledge of the intensity contained in the transmitted beam, unobtainable due to the beam stop. Second, from the results shown in Figure 1c, the ratio of peak positions for the graphene phase (peaks I and II) maintains the value $\sqrt{3}$ (with absolute deviation due to thermal expansion of less than 0.1%), as would be expected for an ideal hexagonal structure. The thermal evolution of the GMO peaks III and IV, while nearly $\sqrt{3}$ in ratio, deviate 1–2% (depending on temperature) from the ideal hexagonal crystalline symmetry. This deviation from hexagonal symmetry, too large to be associated with thermal expansion, clearly indicates that the crystalline phase associated with the diffraction rings III and IV is centered rectangular, albeit nearly hexagonal (quasi-hexagonal), and is distinct from the graphene phase characterized by diffraction rings I and II.

To elucidate the *in situ* SAED observations, we further investigated the geometrical bonding of the films before and after annealing by IRMS. Using two experimental geometries with well-defined polarizations—normal incidence (NI) transmission

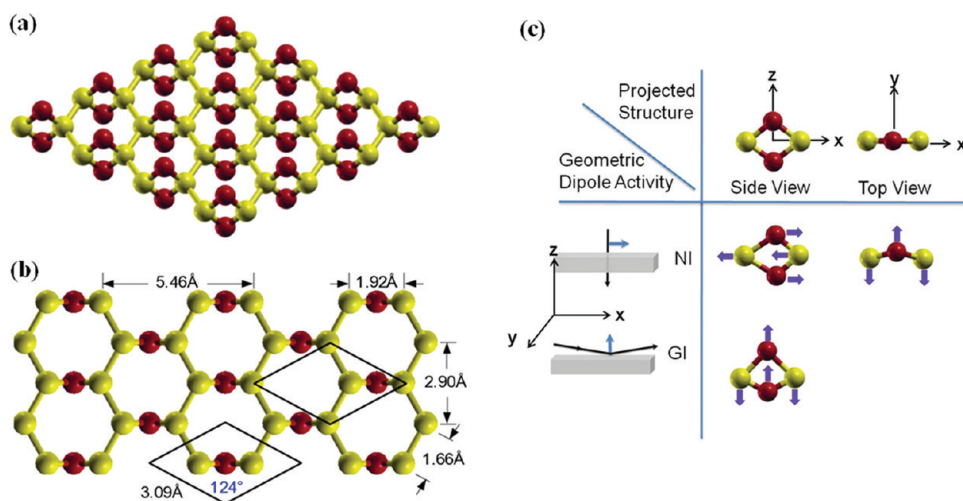


Figure 3. Proposed GMO structure. (a) Perspective view of 4×4 unit cells. Carbon (oxygen) atoms are yellow (red). (b) Top view of GMO with the unit cell and various calculated structural parameters. (c) Schematic of the IR active vibrational modes for this model. Two modes produce a dipole moment within the carbon basal planes, and one mode produces a dipole moment perpendicular to the basal planes and are thus active in the NI and GI geometry, respectively.

and grazing incidence (GI) reflectance—vibrational modes with dynamic dipole moments parallel or perpendicular to the basal plane of the films, respectively, are resolved. Figure 2a–d show the IR absorbance of the samples before and after annealing as measured in NI and GI. The features in the NI spectrum of G-O (Figure 2a) indicate the presence of oxygen functional groups including hydroxyl (3300 cm^{-1}), carbonyl (1708 cm^{-1}), carboxyl (1425 cm^{-1}), epoxide (1245 cm^{-1} , 900 cm^{-1}), and alkoxy (1080 cm^{-1}), consistent with the literature.¹⁹ The feature at 1580 cm^{-1} is assigned to the C=C stretch of the underlying carbon lattice which is activated in G-O due to oxygen functional groups and defects. The GI IR (Figure 2c) absorbance spectrum of G-O also indicates the presence of O–H from intercalated water (stretching modes at $3300\text{--}3600\text{ cm}^{-1}$, bending mode at 1645 cm^{-1}), as well as carbonyl ($1,708\text{ cm}^{-1}$) and hydroxyl (C–OH stretching at 1070 cm^{-1}).

After annealing, many of the oxygen functionalities including carbonyl, carboxyl, alkoxy, and hydroxyl are no longer present in the NI IR spectrum of TRG-O (Figure 2b). The C=C stretching mode softens in frequency and evolves into an asymmetric Fano²⁰ line shape, indicating a continuum of electronic transitions with symmetries parallel to the C=C vibrational excitation spanning at least $0.18\text{--}0.21\text{ eV}$. The C=C stretching mode, which is inactive in pure graphene and graphite due to symmetry considerations, is activated due to defects and neighboring oxidized regions. The C–O–C asymmetric stretching mode, whose overall intensity increases dramatically, is softened by about 25 cm^{-1} . Analysis of this mode from the same position of the same sample before and after annealing showed that the integrated intensity of the C–O–C asymmetric stretching band increased by a factor of

approximately 20 cm^{-1} after the annealing process. The doublet assigned to C–O–C bending has diminished intensity and only appears as a single peak in the annealed spectrum. GI IR absorption spectra from samples after annealing are also shown in Figure 2d, where many oxygen features are missing, including, notably, those associated with water. While the C–O–C mode at 1205 cm^{-1} is very weakly active in this geometry, a prominent new mode is seen at 1050 cm^{-1} . Thus, we conclude that the nanocrystalline phase contains structures that give rise to only two distinct vibrational modes involving C–O displacements that were active in the NI geometry and one C–O mode that was active in the GI geometry.

The electron diffraction data presented in Figure 1 show that the vacuum thermal reduction of multilayered G-O results in a two-phase nanoscale system containing regions of graphene and a new (as yet undetermined) crystalline phase. Phase segregation has been theoretically predicted²¹ and experimentally observed in reduced graphene oxide but with little information provided about the structure.²² In this reference, a C:O ratio of 2:1 was observed through XPS measurements, with slowly varying stoichiometry across the sample. From the IR results above, we establish that this new phase is an ordered solid-state carbon oxide, with exactly three IR active normal modes of vibration involving C–O–C atomic displacements. An extensive search of possible unit cells for C–O–C groups bonded to a primarily unperturbed graphene lattice concluded that no configuration of epoxide groups attached to such a graphene lattice produces SAED reflections in agreement with those measured. Moreover, careful examination of high camera length diffraction patterns from the carbon oxide phase, which probes reciprocal spacings closer to the

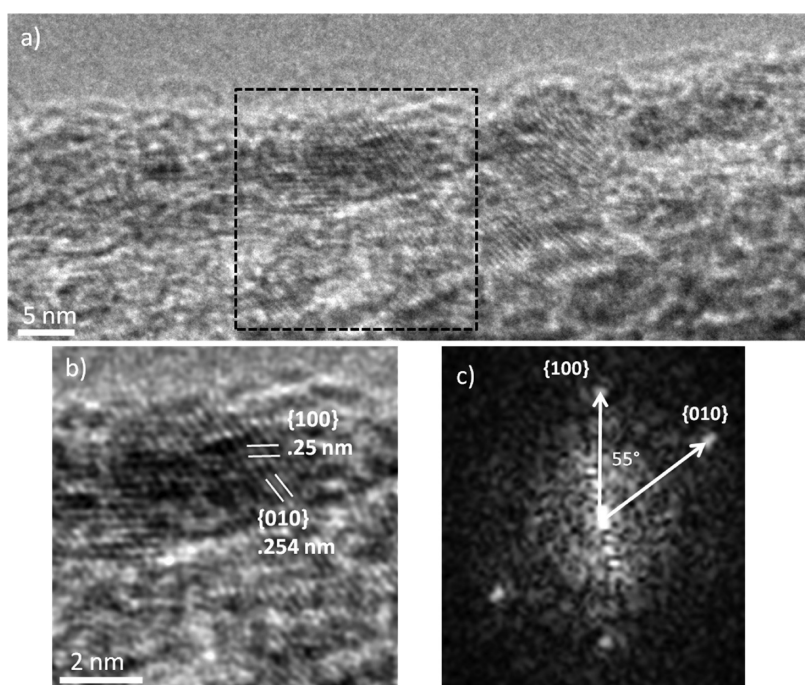


Figure 4. HRTEM images of a TRG-O film. (a) HRTEM image of a thin region of the sample. (b) Enlargement of the marked region from the image in (a) illustrating a GMO domain with denoted lattice spacings (high frequency noise has been filtered out as described in the main text). (c) Numerical diffractogram from the indicated region in (a), showing two prominent reflections with measured spacings in agreement with the GMO {100}- and {010}-type reflections. The measured angle between the spots is 55°.

origin, indicates that the 0.260 nm spacing is the lowest order reflection of the crystalline unit cell, corresponding to a unit cell about 20% larger than graphene. Therefore, our electron diffraction data indicate a quasi-hexagonal unit cell (Table S2, Note S1).

Indeed, our DFT calculations demonstrate that adding oxygen to graphene is energetically favorable, leading to the proposed quasi-hexagonal double-epoxide structure (Figure 3a–b; C:O = 1:1) with a binding energy of 4.36 eV/O. This is significantly higher than previously reported GO configurations with high epoxide coverage,²³ where ordered epoxide groups in a C₂O structure yield a binding energy of 3.73 eV/O in our calculation. This structure has some similarities to models proposed in previous calculations.²⁴ The calculated lattice parameters of this centered-rectangular (quasi-hexagonal) structure are given in Figure 3b. Compared with graphene, the magnitude of the primitive lattice vectors increases to 3.09 Å (from 2.46 Å) and the angle between them is 124° versus the 120° of an ideal hexagonal lattice. Although this structure no longer has the 3-fold symmetry of the graphene lattice, there are three sets of mirror planes, corresponding to *D*_{2h} symmetry, which implies that there are three IR-active vibrational modes (Figure 3c), two C–O–C modes in NI and one C–O–C mode in GI (Supporting Information for details), as observed experimentally. Various configurations of C–O–C groups were considered; however, only the double-epoxide structure produces

the correct number of allowed vibrational modes in each experimental geometry. Thus, the structure suggested by DFT calculation is consistent with the experimental diffraction and infrared spectroscopic data. The O to C ratio in the oxidized regions is significantly higher than previously reported values in unreduced multilayer G-O where the average chemical compositions vary from C₁O_{0.17}H_{0.08} to C₁O_{0.49}H_{0.2} depending on the oxidation time and methods.^{25,26} As graphene-like islands spread across the G-O film,²¹ the local oxidation level has been reported to be as high as C₁O_{0.5} to C₁O_{0.75}H_{0.75} for monolayer G-O.²³ Here, the higher ratio of 1:1 can be realized by converting oxygen species present initially in G-O to the double-epoxide structure. Initially, there are not enough epoxide or cyclic ether-type oxygen groups in G-O to create GMO. However, conversion of the remaining oxygen-containing functional groups to a C–O–C configuration could provide a viable path. The spectroscopic evidence that suggests this transformation is the changes of the integrated intensities of all the oxygen-containing functional groups before and after annealing, including the absence of the H₂O, OH, and carbonyl absorption bands and the increase in the C–O–C asymmetric stretching peak (Figure 2b) after annealing. Meanwhile, experimentally we observe an increase in diffracted intensity of the original G-O/graphene reflections, which indicates a concurrent increase in the crystalline areas of graphene-like

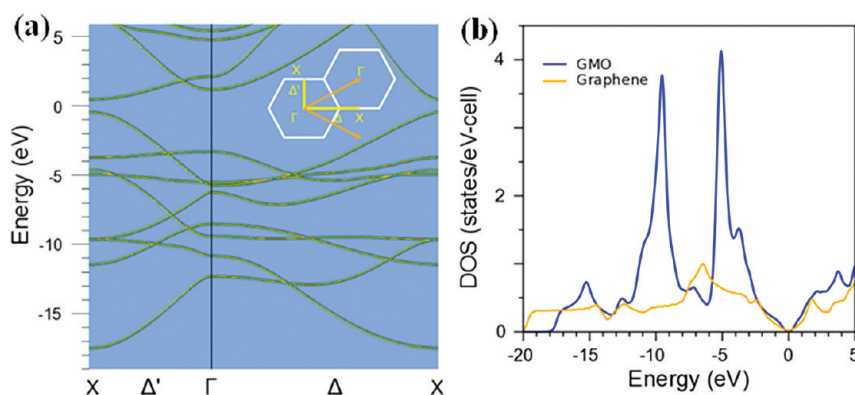


Figure 5. Calculated band structure and density of states (DOS) for GMO. (a) Band structure along the high symmetry directions (inset). (b) Comparison of DOS for GMO and graphene.

islands that are oxygen-free regions. We emphasize that the increase in stoichiometry is only localized to small crystalline regions of GMO and that the overall oxygen content of the entire sample has not increased. The formation of the new composite nanomaterial is likely a consequence of the large number of layers in the starting material and the diffusion-limited nature of the reduction process. When similar *in situ* vacuum annealing experiments were performed on a monolayer G-O sample, the GMO phase was not observed (Figure S4).

The proposed structural model was further investigated using HRTEM. While the majority of the sample was much too thick to obtain atomic resolution images, we were able to locate a very thin region where the TRG-O sheets tore during annealing that enabled imaging of the lattice planes of individual GMO domains. HRTEM images of such a region are shown in Figure 4. The HRTEM image in Figure 4a shows that lattice fringes from individual GMO domains can be resolved in thin regions of the sample edges. Figure 4b shows an enlargement of a single GMO domain from the HRTEM image in Figure 4a, with the numerical diffractogram from the same region shown in Figure 4c. In Figure 4b, high frequency components of the image beyond the lattice resolution of the microscope have been filtered out, as these data contain no real information. In the diffractogram of this region, two reflections are observed with measured spacings of 0.25 and 0.254 nm, corresponding to both the {100}- and {010}-type reflections of GMO. Measurement of the angle between the sets of lattice fringes yields an angle of 55°. This is in excellent agreement with DFT predictions from the relaxed GMO model structure which suggests an angle of 56° between the GMO {100} and {010} planes. These results further confirm the structural conclusions based on all SAED, IRMS, and DFT analyses.

The new GMO is predicted to be a semiconductor, with a direct band gap of ~0.9 eV at the X point

(Figure 5). The size (and existence) of the gap is dependent on the distortion of the lattice away from the ideal hexagonal lattice: constraining GMO to be hexagonal (i.e., an angle of 120°) results in a zero gap semiconductor. The overall shapes and magnitudes of the density of states (DOS) of GMO and graphene within ± 2 eV of the Fermi level (beyond the gap) are very similar. The sensitivity of the electronic properties to subtle changes in the structure could potentially lead to the ability to tailor the band gap. In spite of the predicted semiconducting nature of GMO, transport measurements (Figure S5) show that the resistivity of as-reduced TRG-O (GMO and graphene complex) is several orders of magnitude lower than unreduced G-O, suggesting that islands of GMO that are interspersed among the graphene-like regions do not destroy the graphene connectivity completely. Our preliminary results suggest that final graphene/GMO relative quantities and hence the connectivity of graphene regions are highly dependent on the ultimate annealing time and temperature, with different products demonstrating strong sensitivity on these parameters. This is not surprising considering previous studies of the evolution of electrical conductivity during *in situ* thermal reduction of monolayer GO,²⁷ which demonstrate a complicated time and temperature dependence of the oxidation and hence conductivity. These characteristics warrant further investigation, and further reports on the electrical properties of the TRG-O composite materials will be forthcoming.

CONCLUSIONS

In summary, we have demonstrated that the vacuum thermal reduction of multilayer G-O films yields a composite material containing graphene and graphene monoxide nanocrystalline regions. The atomic structure of GMO, consistent with all experimental evidence from electron diffraction and IRMS, possesses an O:C = 1:1 stoichiometry, with double-epoxide GMO units arranged on a 2D quasi-hexagonal lattice. Crystalline CO has never been observed in nature at standard

temperature and pressure, making solid GMO a significant discovery. The semiconducting properties of GMO, predicted by *ab initio* calculations, suggest that this new material might be useful for various electronic applications such as sensors, transistors, and optoelectronic

devices, particularly considering its compatibility with graphene. This discovery of nanocrystalline GMO is a critical step to seeking methods to develop band gap controlled, crystalline, monolayered graphene oxide that do not rely on multilayered materials.

METHODS

TEM Sample Preparation. G-O suspensions were synthesized using a modified Hummers method, as described by our collaborators.²⁸ G-O multilayer samples were prepared by drop-casting 2 μ L of the resulting suspension onto bare 200 mesh Mo TEM grids. The individual G-O monolayers became stacked after water evaporation, forming self-supporting multilayer structures that span the grid holes. Monolayer GO samples were prepared by drop-casting diluted suspensions into Si TEM grids with an ultrathin Si₃N₄ membrane.

TEM Measurements. TEM studies were performed *in situ* using a Gatan tantalum-cup heating holder inside a Hitachi H9000NAR TEM operating at an accelerating voltage of 300 keV. The column pressure of the TEM was maintained at approximately 10⁻⁷ Torr. The TEM is equipped with a Gatan Orius SC CCD, which was used to record diffraction movies with 1 frame (1 s exposure time) per 4 s. An SAED pattern of the G-O film was recorded during the vacuum annealing process, allowing the structure to be correlated with temperature that was detected with a thermocouple. An SAED movie (see Supporting Information) was recorded at the same region of the sample, and the electron beam intensity was fixed throughout the experiment. Importantly, SAED patterns were recorded both during and after annealing of the sample, indicating that the structural changes observed during the experiment were stable upon cooling the sample to room temperature. A radially averaged profile of diffraction intensity (such as displayed in the insets of Figure 1a) was extracted from each frame of the SAED movie corresponding to the temperature of the sample and subsequently combined as Figure 1b, thus indicating the evolution of the reciprocal space positions (y-axis) of the diffracted electrons with increasing temperature (x-axis). During annealing and after being cooled, the samples were studied using SAED, CBED, HRTEM, and bright-field TEM. In other *in situ* experiments, a CBED pattern, taken with a 17 nm convergent beam electron probe, was examined as the samples were reduced.

IRMS Measurements. After TEM analysis, IRMS was performed on the same TRG-O samples. IR measurements were performed at the Synchrotron Radiation Center (SRC, Stoughton, WI) at the IRENI beamline.²⁹ The films as prepared on TEM grids were measured in a Bruker Hyperion 3000 IR Microscope coupled to a synchrotron source. Normal incidence transmittance and reflectance measurements were performed on the *free-standing* films supported on TEM grids. By repeating the experiments with objectives of varying numerical aperture, measurement effects resulting from convergence of the synchrotron beam being focused by the Schwarzschild focusing optics were ruled out. The films were subsequently removed from the grids and placed on microscope slides with an IR reflective coating (Kevley Technologies). This enabled the films to be measured at a grazing incidence using a Bruker Grazing Angle IR microscope objective lens. GI measurements were performed with an IR polarizer to emphasize only radiation polarized parallel to the plane of incidence.

DFT Calculations. The density functional calculations were carried out using the all-electron Full-potential Linearized Augmented Plane Wave method, as implemented in flair.³⁰ The GMO and graphene calculations used the generalized gradient approximation (GGA) of Perdew, Burke, and Ernzerhof for exchange correlation; sphere radii of 1.2 a_B for both C and O; plane wave basis and charge/potential representation cutoffs of 275 and 2700 eV, respectively; 12 × 12 × 2 to 36 × 36 × 2 k-point sets; and vacuum regions of 15 Å. The internal

coordinates were relaxed to a force criterion of 10⁻⁴ eV/Å. Other C:O ratios and configurations were modeled starting from 2 × 2 hexagonal cells with eight carbon atoms.

Acknowledgment. This work was supported by the NSF (CMMI-0856753 and CMMI-0900509). This work is based upon experiments performed at the Synchrotron Radiation Center. The SRC is funded by the NSF under Award No. DMR-0537588. Work performed at the SRC IRENI beamline been done with support from an NSF Major Research Instrumentation grant (DMR-0619759). The authors thank Bruker Technologies for the Grazing Angle Objective used for this work.

Supporting Information Available: Supplementary data including detailed SAED analysis of low and high order reflections of G-O and TRG-O, *in situ* CBED experiments on G-O and TRG-O, determination of IR activity of GMO, *in situ* SAED experiments with a G-O monolayer, and electrical transport measurements are presented. This material is available free of charge via the Internet at <http://pubs.acs.org>.

REFERENCES AND NOTES

- Novoselov, K. S.; Geim, A. K.; Morozov, S. V.; Jiang, D.; Zhang, Y.; Dubonos, S. V.; Grigorieva, I. V.; Firsov, A. A. Electric Field Effect in Atomically Thin Carbon Films. *Science* **2004**, *306*, 666–669.
- Li, D.; Kaner, R. B. Materials Science - Graphene-Based Materials. *Science* **2008**, *320*, 1170–1171.
- Zhang, Y. B.; Tan, Y. W.; Stormer, H. L.; Kim, P. Experimental Observation of the Quantum Hall Effect and Berry's Phase in Graphene. *Nature* **2005**, *438*, 201–204.
- Dikin, D. A.; Stankovich, S.; Zimney, E. J.; Piner, R. D.; Dommett, G. H. B.; Evmenenko, G.; Nguyen, S. T.; Ruoff, R. S. Preparation and Characterization of Graphene Oxide Paper. *Nature* **2007**, *448*, 457–460.
- Dreyer, D. R.; Ruoff, R. S.; Bielawski, C. W. From Conception to Realization: An Historical Account of Graphene and Some Perspectives for Its Future. *Angew. Chem., Int. Ed.* **2010**, *49*, 9336–9344.
- Dreyer, D. R.; Park, S.; Bielawski, C. W.; Ruoff, R. S. The Chemistry of Graphene Oxide. *Chem. Soc. Rev.* **2010**, *39*, 228–240.
- Li, D.; Muller, M. B.; Gilje, S.; Kaner, R. B.; Wallace, G. G. Processable Aqueous Dispersions of Graphene Nano-sheets. *Nat. Nanotechnol.* **2008**, *3*, 101–105.
- Gao, W.; Alemany, L. B.; Ci, L. J.; Ajayan, P. M. New Insights into the Structure and Reduction of Graphite Oxide. *Nat. Chem.* **2009**, *1*, 403–408.
- Zhu, Y.; Murali, S.; Stoller, M. D.; Ganesh, K. J.; Cai, W.; Ferreira, P. J.; Pirkle, A.; Wallace, R. M.; Cychosz, K. A.; Thommes, M.; et al. Carbon-Based Supercapacitors Produced by Activation of Graphene. *Science* **2011**, *332*, 1537–1541.
- Lu, G. H.; Park, S.; Yu, K. H.; Ruoff, R. S.; Ocola, L. E.; Rosenmann, D.; Chen, J. H. Toward Practical Gas Sensing with Highly Reduced Graphene Oxide: A New Signal Processing Method to Circumvent Run-to-Run and Device-to-Device Variations. *ACS Nano* **2011**, *5*, 1154–1164.
- Mao, S.; Lu, G. H.; Yu, K. H.; Bo, Z.; Chen, J. H. Specific Protein Detection Using Thermally Reduced Graphene Oxide Sheet Decorated with Gold Nanoparticle-Antibody Conjugates. *Adv. Mater.* **2010**, *22*, 3521–3526.

12. Eda, G.; Fanchini, G.; Chhowalla, M. Large-Area Ultrathin Films of Reduced Graphene Oxide as a Transparent and Flexible Electronic Material. *Nat. Nanotechnol.* **2008**, *3*, 270–274.
13. Mkhoyan, K. A.; Contryman, A. W.; Silcox, J.; Stewart, D. A.; Eda, G.; Mattevi, C.; Miller, S.; Chhowalla, M. Atomic and Electronic Structure of Graphene-Oxide. *Nano Lett.* **2009**, *9*, 1058–1063.
14. Wilson, N. R.; Pandey, P. A.; Beanland, R.; Young, R. J.; Kinloch, I. A.; Gong, L.; Liu, Z.; Suenaga, K.; Rourke, J. P.; York, S. J.; et al. Graphene Oxide: Structural Analysis and Application as a Highly Transparent Support for Electron Microscopy. *ACS Nano* **2009**, *3*, 2547–2556.
15. Acik, M.; Lee, G.; Mattevi, C.; Chhowalla, M.; Cho, K.; Chabal, Y. J. Unusual Infrared-Absorption Mechanism in Thermally Reduced Graphene Oxide. *Nat. Mater.* **2010**, *9*, 840–845.
16. Bagri, A.; Mattevi, C.; Acik, M.; Chabal, Y. J.; Chhowalla, M.; Shenoy, V. B. Structural Evolution During the Reduction of Chemically Derived Graphene Oxide. *Nat. Chem.* **2010**, *2*, 581–587.
17. Acik, M.; Mattevi, C.; Gong, C.; Lee, G.; Cho, K.; Chhowalla, M.; Chabal, Y. J. The Role of Intercalated Water in Multi-layered Graphene Oxide. *ACS Nano* **2010**, *4*, 5861–5868.
18. Lopez, V.; Sundaram, R. S.; Gomez-Navarro, C.; Olea, D.; Burghard, M.; Gomez-Herrero, J.; Zamora, F.; Kern, K. Chemical Vapor Deposition Repair of Graphene Oxide: A Route to Highly Conductive Graphene Monolayers. *Adv. Mater.* **2009**, *21*, 4683–4686.
19. Stankovich, S.; Dikin, D. A.; Dommett, G. H. B.; Kohlhaas, K. M.; Zimney, E. J.; Stach, E. A.; Piner, R. D.; Nguyen, S. T.; Ruoff, R. S. Graphene-Based Composite Materials. *Nature* **2006**, *442*, 282–286.
20. Fano, U. Effects of Configuration Interaction on Intensities and Phase Shifts. *Phys. Rev.* **1961**, *124*, 1866.
21. Erickson, K.; Erni, R.; Lee, Z.; Alem, N.; Gannett, W.; Zettl, A. Determination of the Local Chemical Structure of Graphene Oxide and Reduced Graphene Oxide. *Adv. Mater.* **2010**, *22*, 4467–4472.
22. Ekiz, O. O.; Urel, M.; Guner, H.; Mizrak, A. K.; Dana, A. Reversible Electrical Reduction and Oxidation of Graphene Oxide. *ACS Nano* **2011**, *5*, 2475–2482.
23. Boukhvalov, D. W.; Katsnelson, M. I. Modeling of Graphite Oxide. *J. Am. Chem. Soc.* **2008**, *130*, 10697–10701.
24. Xiang, H. J.; Wei, S. H.; Gong, X. G. Structural Motifs in Oxidized Graphene: A Genetic Algorithm Study Based on Density Functional Theory. *Phys. Rev. B* **2010**, *82*, 035416.
25. Cassagneau, T.; Guerin, F.; Fendler, J. H. Preparation and Characterization of Ultrathin Films Layer-by-Layer Self-Assembled from Graphite Oxide Nanoplatelets and Polymers. *Langmuir* **2000**, *16*, 7318–7324.
26. Szabo, T.; Berkesi, O.; Forgo, P.; Josepovits, K.; Sanakis, Y.; Petridis, D.; Dekany, I. Evolution of Surface Functional Groups in a Series of Progressively Oxidized Graphite Oxides. *Chem. Mater.* **2006**, *18*, 2740–2749.
27. Jung, I.; Dikin, D.; Park, S.; Cai, W.; Mielke, S. L.; Ruoff, R. S. Effect of Water Vapor on Electrical Properties of Individual Reduced Graphene Oxide Sheets. *J. Phys. Chem. C* **2008**, *112*, 20264–20268.
28. Park, S.; An, J. H.; Piner, R. D.; Jung, I.; Yang, D. X.; Velamakanni, A.; Nguyen, S. T.; Ruoff, R. S. Aqueous Suspension and Characterization of Chemically Modified Graphene Sheets. *Chem. Mater.* **2008**, *20*, 6592–6594.
29. Nasse, M. J.; Walsh, M. J.; Mattson, E. C.; Reininger, R.; Kajdacsy-Balla, A.; Macias, V.; Bhargava, R.; Hirschmugl, C. J. High-Resolution Fourier-Transform Infrared Chemical Imaging with Multiple Synchrotron Beams. *Nat. Methods* **2011**, *8*, 413–416.
30. Weinert, M.; Schneider, G.; Podloucky, R.; Redinger, J. Flapw: Applications and Implementations. *J. Phys.: Condens. Matter* **2009**, *21*, 084201.